

Rare-metal mineralization and crust-derived magmatism in a collisional orogen: the Variscan metallogenic odyssey of the Sioule region (French Massif Central)

Christophe Ballouard ^{a,*}, Patrick A. Carr ^a, Loïs Monnier ^b, Jean-Charles Fidalgo ^a, Océane Rocher ^a, Nicolas Esteves ^c, Oscar Laurent ^b, Marie Daoulas-Gérardin ^a, Chantal Peiffert ^a, Julien Mercadier ^a, Alexis Plunder ^d, Jérémie Melleton ^d

*christophe.ballouard@univ-lorraine.fr

^a Université de Lorraine, CNRS, GeoRessources, F-54506, Vandoeuvre-lès-Nancy, France

^b CNRS, Géosciences Environnement Toulouse (GET), Observatoire Midi-Pyrénées, 31400 Toulouse, France

^c Université de Lorraine, CNRS, CRPG, F-54000 Nancy, France

^d BRGM, F-45060 Orléans, France

Supplementary Material

Analytical protocol

Whole-rock geochemistry

Samples were crushed to obtain adequate powder fractions using an agate mill. Geochemical analyses were performed by the Service d'Analyses des Roches et Minéraux (SARM, CRPG-CNRS, Vandoeuvre-Lès-Nancy, France) using inductively coupled plasma atomic emission spectroscopy (AES) for major elements, inductively coupled plasma mass spectrometry (ICP-MS) for trace elements, absorptiometry for B, flame atomic absorption spectrometry (AAS) for Li and potentiometry for F (Carignan et al., 2001). All data along with sample GPS coordinates are provided in the [Supplementary Tables](#).

Mineral separation

Zircon were concentrated using facilities available at GeoRessources laboratory of the University of Lorraine (Vandoeuvre-Lès-Nancy, France). Rocks were crushed and only the fraction with a diameter <250 µm was kept. Heavy minerals were mostly concentrated using panning, although heavy liquids were used for one sample with low amount of zircon (ECH22-02). Zircon grains were

handpicked under a binocular microscope and embedded in epoxy mounts before being hand-grounded and polished on a lap wheel.

Mineral imaging

Mineral imaging on thin sections, thick sections or grains mounts, was dominantly performed at the GeoRessources laboratory.

Micro-X-Ray Fluorescence (μ -XRF) analyses of thick sections were carried out with a Bruker M4 Tornado μ -XRF benchtop spectrometer. X-ray maps were acquired with a dwell time of 12 ms per pixel and a spacing of 25 μ m between each point.

Cathodoluminescence (CL) imaging of zircon was performed on a NewTec scientific Cathodyne connected to a Leica DM2700 M optical microscope to reveal the distinct micro-textural domains which were further analyzed. CL study of apatite was performed using either an OPEA Cathodyne connected to a Nikon Eclipse LV100 microscope at GeoRessources or a Tescan Vega4 scanning electron microscope (SEM) at Géosciences Environnement Toulouse (GET). The CL images of cassiterite were obtained using a Tescan Vega4 SEM at GeoRessources. Wolframite grains were imaged using backscattered electron (BSE) microscopy and qualitative energy-dispersive X-ray (EDX) mapping with a Tescan Vega4 SEM.

U-Pb geochronology

U-Pb dating was conducted on the LA-ICP-MS platform at GeoRessources. Cassiterite, wolframite, and apatite U-Pb analyses were performed using an ESI NWR193UC excimer laser equipped with a two-volume ablation chamber coupled to a Nu Instruments AttoM™ ES sector field ICP-MS. Zircon U-Pb and trace element analyses were performed using the same laser ablation system; however, analyses conducted between May and mid-June 2023 employed an Agilent 8900 quadrupole ICP-MS, while subsequent U-Pb analyses (from mid-June 2023 to September 2024) utilized the AttoM™ ES. Details of the laser and ICP-MS systems, as well as their operating conditions, are provided in the [Supplementary Tables](#), along with U-Pb data for samples and reference materials.

For all minerals, the ablated material was transported in a helium carrier gas (flow rate 0.65–0.75 L/min), then mixed with nitrogen (0.003 L/min) and argon (0.4 L/min for the AttoM™ ES and 0.9 L/min for the Agilent 8900) before being

injected into the plasma source. Gas flow rates, including the Ar(-N₂) plasma make-up gas, and ion lens parameters were optimized on the NIST SRM612 glass standard to maximize sensitivity, maintain low oxide levels (ThO/Th < 0.05%), and minimize Th/U fractionation (typically 0.94–0.99).

Wolframite was analysed directly on a thin section using a laser spot size of 90 µm, a fluence of ~5 J.cm⁻² over 40 s with a repetition rate of 7 Hz. Cassiterite was analysed in thin sections or on grain mounts (i.e. Beauvoir RMG cassiterite). Laser operating conditions consisted of an 80 µm spot size, a repetition rate of 7 Hz and an energy density between 4.0 and 7.0 J.cm⁻² over 40 s. Analyses followed the protocols of Carr et al. (2021) for wolframite and Carr et al. (2023) for cassiterite. The following isotopes were measured (with integration time in parentheses): ²⁰²Hg (10 ms), ²⁰⁴Pb (10 ms), ²⁰⁶Pb (10 ms), ²⁰⁷Pb (50 ms), ²⁰⁸Pb (10 ms), ²³²Th (10 ms), ²³⁵U (10 ms), and ²³⁸U (10 ms). Measured U-Pb and Pb-Pb isotopic ratios were corrected for instrument mass fractionation (IMF) in Iolite4 (Paton et al., 2010) using the VizualComPbine DRS (Petrus and Kamber, 2012), with either the homemade wolframite reference material 14-MP-28 (158.14 ± 1.95 Ma) or the Yankee cassiterite (246.48 ± 0.51 Ma; Carr et al., 2020) used as the primary reference material for U/Pb ratios, along with NIST SRM614 for Pb/Pb ratios (Woodhead and Hergt, 2000). During the analytical sessions, the PO-10-2 wolframite (324.63 ± 2.07 Ma) and Jian-1 cassiterite (154.969 ± 0.082 Ma; Tapster and Bright, 2020), yielded lower intercept ages of 332.5 ± 8.4 Ma and 154.63 ± 3.1 Ma, respectively. Both ages are consistent with their recommended values, considering the long-term reproducibility precision of the cassiterite control material, estimated at 1.9% (Carr et al., 2023) that was propagated in quadrature to the unknowns for both cassiterite and wolframite.

Laser ablations of apatite were carried out with a spot size of 30 µm, repetition rate of 7 Hz, laser energy density of ca. 2 J.cm⁻², and a sampling period of 30 s, following the analytical protocol described in Rocher et al. (2024). The analysed isotopes (and their integration times) were the same as those used for wolframite and cassiterite, and the U-Pb data reduction was performed with Iolite and the “U-Pb Geochronology” data reduction scheme (Paton et al., 2010). ²⁰⁷Pb/²⁰⁶Pb and ²³⁸U/²⁰⁶Pb ratios were first normalised to the NIST SRM 610 glass in Iolite (Jochum et al., 2011; Woodhead and Hergt, 2000). ²³⁸U/²⁰⁶Pb ratios were then corrected for the apatite-glass matrix effect in Excel by applying an average correction factor determined based on the offset between measured and

reference lower intercept dates of matrix-matched reference materials: the Madagascar apatite (assumed age of 479 Ma; the mid-point between the two ages reported in [Thomson et al., 2012](#)), the McClure Mountain apatite (U-Pb age of 523.51 ± 2.09 ; [Schoene and Bowring, 2006](#)) and the Duluth apatite (U-Pb age 1099.1 ± 0.5 Ma; [Schmitz et al., 2003](#)). The Madagascar, McClure and Duluth apatite yielded lower intercept ages of 490.9 ± 5.5 Ma, 512.3 ± 10.5 Ma and 1087.0 ± 23.7 Ma, respectively. The long-term reproducibility precision of the apatite reference materials, estimated at 1.0% ([Rocher et al., 2024](#)), was propagated to the calculated ages.

Zircon grains were ablated using a spot size of 30 μm , a repetition rate of 5 Hz and an energy density between 3 and 4 $\text{J}\cdot\text{cm}^{-2}$. When utilizing the 8900 ICP-MS, the following isotopes were measured (integration time in parentheses): ^7Li (10 ms), ^{27}Al (10ms), ^{29}Si (10 ms), ^{44}Ca (10 ms), ^{49}Ti (25 ms), ^{89}Y (10 ms), ^{91}Zr (10 ms), ^{93}Nb (10 ms), ^{118}Sn (10 ms), ^{139}La (10 ms), ^{140}Ce (10 ms), ^{146}Nd (10 ms), ^{147}Sm (10 ms), ^{153}Eu (10 ms), ^{157}Gd (10 ms), ^{159}Tb (10 ms), ^{163}Dy (10 ms), ^{178}Hf (10 ms), ^{181}Ta (10 ms), ^{182}W (10 ms), ^{202}Hg (10 ms), ^{204}Pb (10 ms), ^{206}Pb (10 ms), ^{207}Pb (50 ms), ^{208}Pb (10 ms), ^{232}Th (10 ms), and ^{238}U (10 ms). When using the AttoM™ ES ICP-MS, the same isotopes and integration times were employed as for cassiterite, wolframite, and apatite. U-Pb data reduction was performed in Iolite using the “U-Pb Geochronology” data reduction scheme, with a primary zircon reference material used to correct both U/Pb and Pb/Pb ratios. During the analytical sessions performed in 2023, the 91500 zircon (1062.4 Ma; [Wiedenbeck et al., 1995](#)) was used as the primary reference material, whereas the RAK-17 zircon (295.56 ± 0.21 Ma; [Webb et al., 2020](#)) was adopted in 2024 due to improved analytical reproducibility. The control materials used to monitor the accuracy of data correction included the Temora-2 ([Black et al., 2004](#)), Peng-16 (159.27 ± 0.07 Ma; [G-Chron-3](#)), 91500, Mud Tank ([Gain et al., 2019](#)), Kara-18 ([Webb et al., 2021](#)) and/or Rak-17 zircon. The long-term reproducibility precision (calculated from Temora-2, 91500, Peng-16 and Rak-17 zircon) ranged from 0.6% to 1.5% ([Fig. S1](#)). A conservative value of 1.5% was propagated in quadrature to the calculated sample ages.

Trace element data reduction was done in Iolite 4, using NIST SRM610 ([Jochum et al., 2011](#)) as the primary reference material and stoichiometric SiO_2 of zircon used as the internal standard. The accuracy and reproducibility of the

corrections were monitored using the NIST612 glass, with deviations from reference values generally below 5%, except for Ti ($\leq 14\%$) and Zr ($\leq 30\%$).

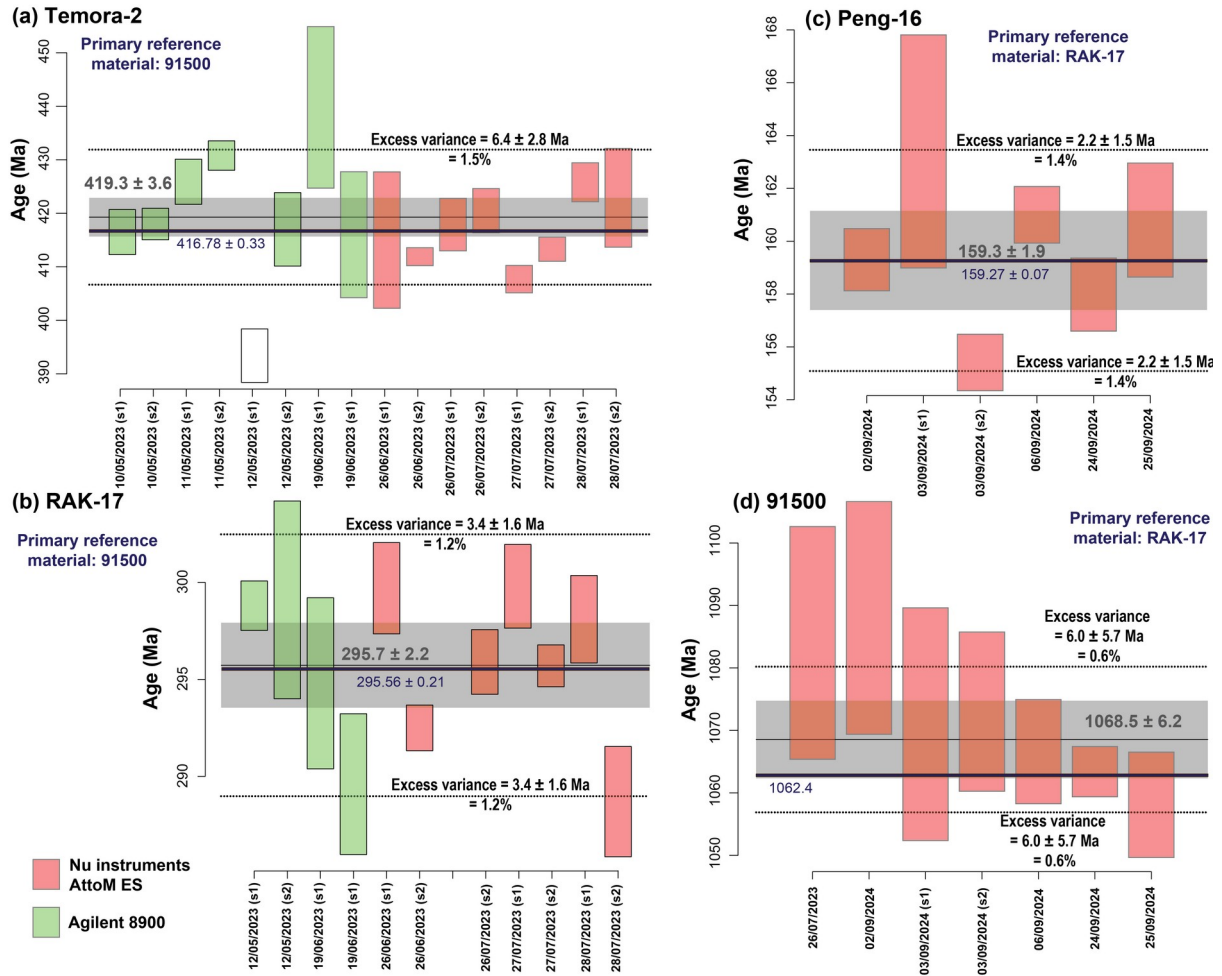


Fig. S1: Summary of U-Pb ages (2σ) obtained on zircon control materials during the different LA-ICP-MS analytical sessions using the Agilent 8900 (green) and Nu Instruments AttoM ES (red) systems at GeoRessources. The zircon primary reference material was changed from 91500 (Wiedenbeck et al., 1995) in 2023 (a-b) to RAK-17 (Webb et al., 2020) in 2024 (c-d). The recommended age of Temora-2 (Black et al., 2004), RAK-17, Peng-16 (G-Chron3) and 91500 are shown in blue, while calculated mean U-Pb ages are shown in grey. The excess variance in U-Pb ages determined across all analytical sessions ranges from 0.6% for 91500 (d) to 1.5% for Temora-2 (a).

Other Supplementary Figures

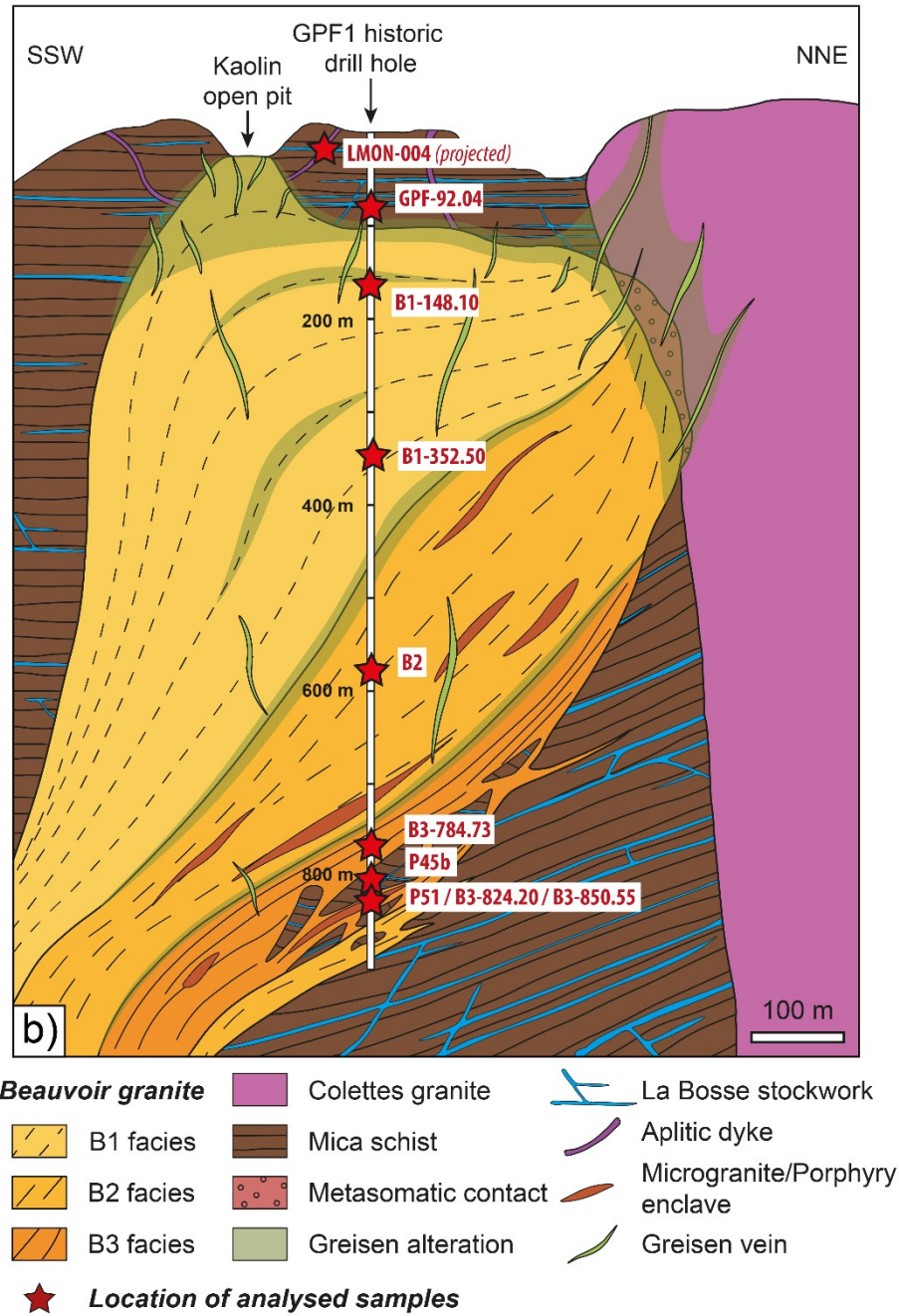


Fig. S2: Interpretative cross section of the Beauvoir rare-metal granite of the Echassières complex (Cuney et al., 1992; Rocher et al., 2024) showing location of analyzed samples.

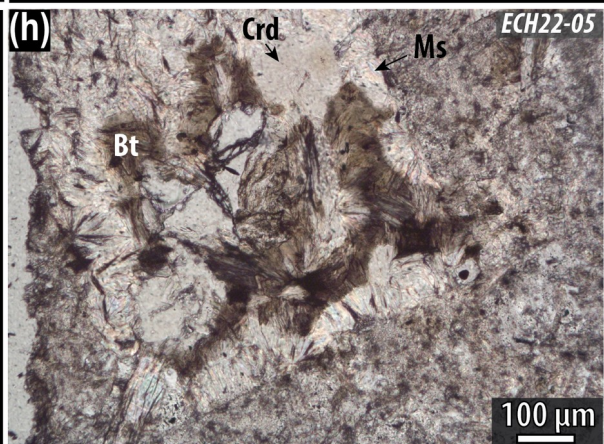
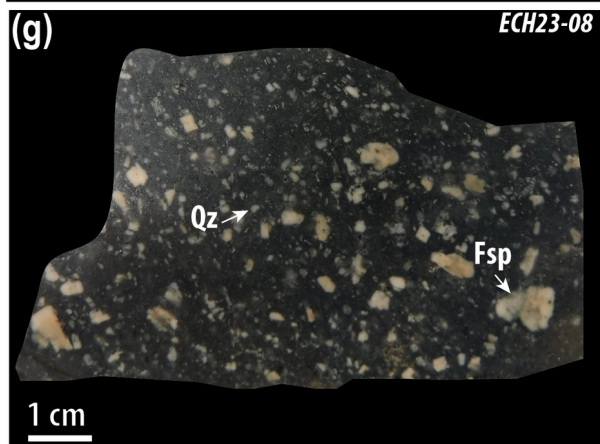
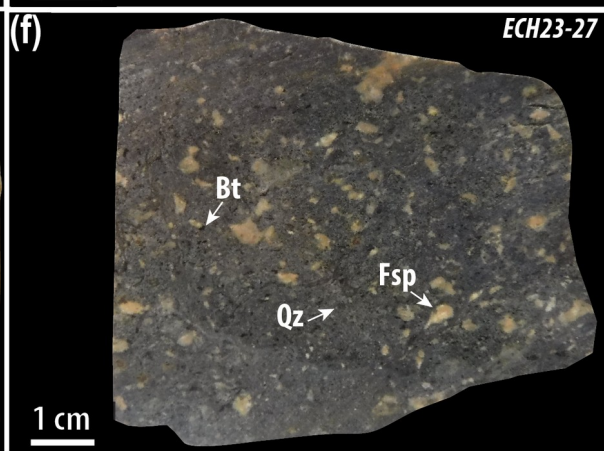
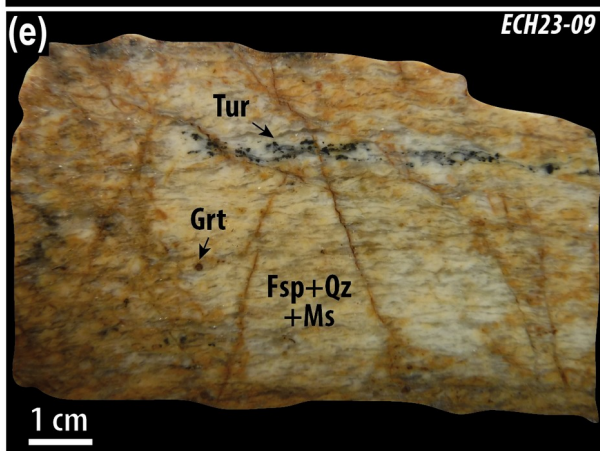
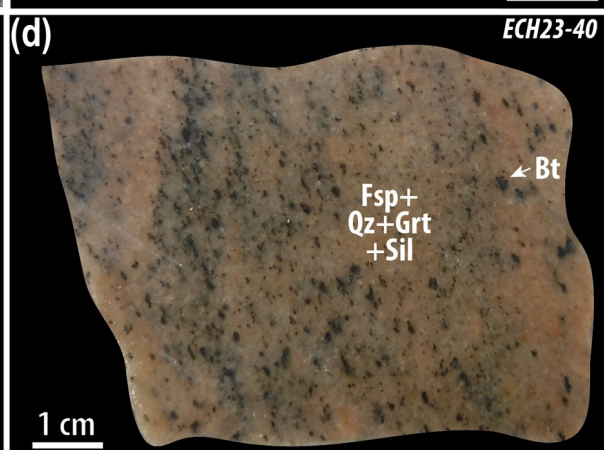
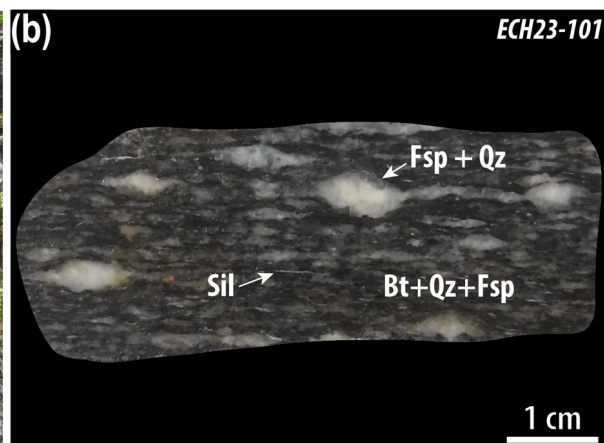
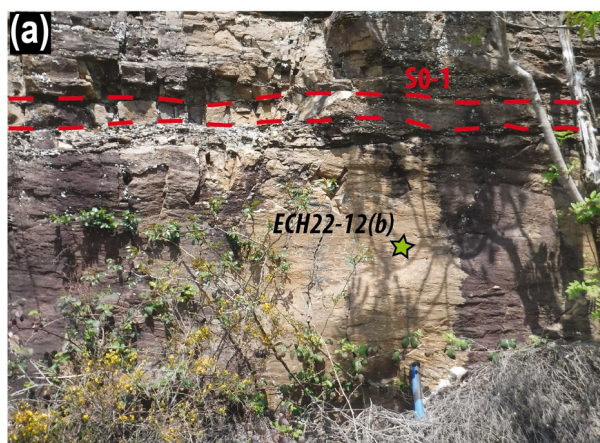


Fig. S3: Supplementary photographs of samples from the Sioule region investigated during this study. (a-b) Metasedimentary rock samples collected for detrital zircon U-Pb geochronology within the paragneiss unit: (a) Quartzite interlayered with migmatitic paragneiss; (b) biotite-sillimanite paragneiss. (c-d) Cambrian metatextitic monzogranitic gneiss and diatextitic leucogranitic gneiss. (e) Fine-grained leucogranite from the Saint-Gervais Massif deformed along the Sainte-Christine shear zone. (f) Trachy-dacitic tuff from the Manzat Formation. (g) Trachy-dacitic tuff from the Châteauneuf Formation. (h) Microphotograph of a cordierite crystal almost entirely replaced by white and black micas in the devitrified matrix of a rhyolitic dyke from the Echassières Complex.

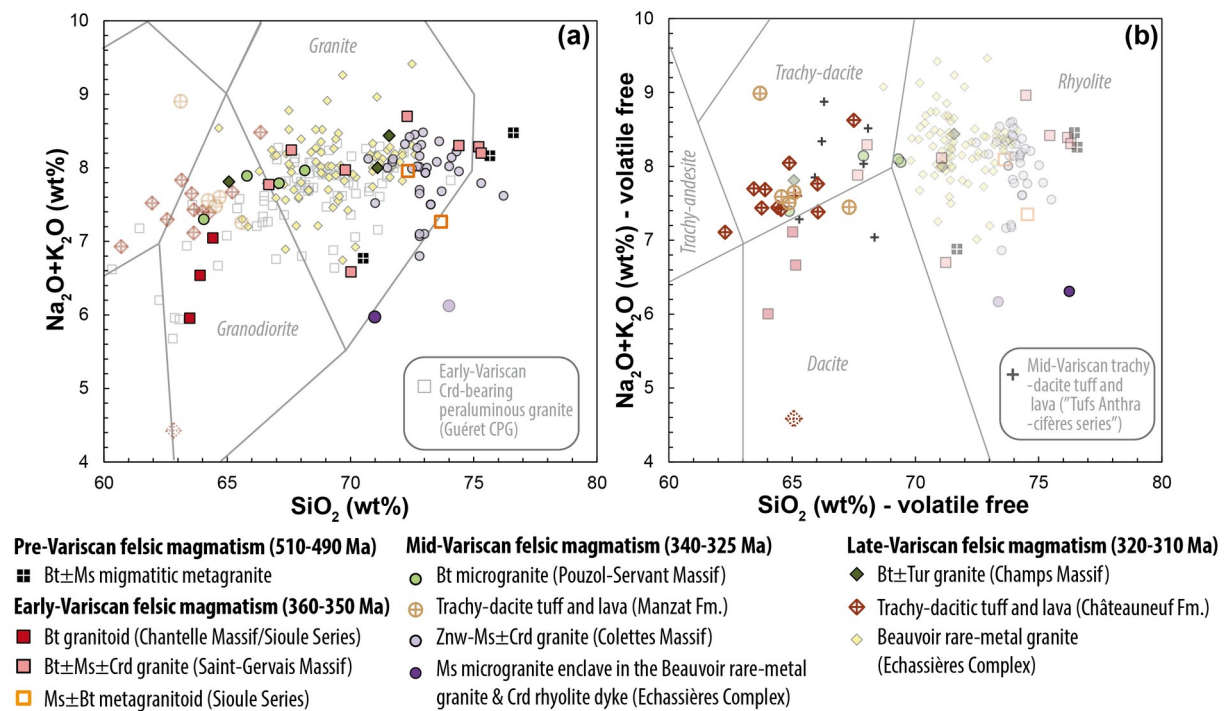
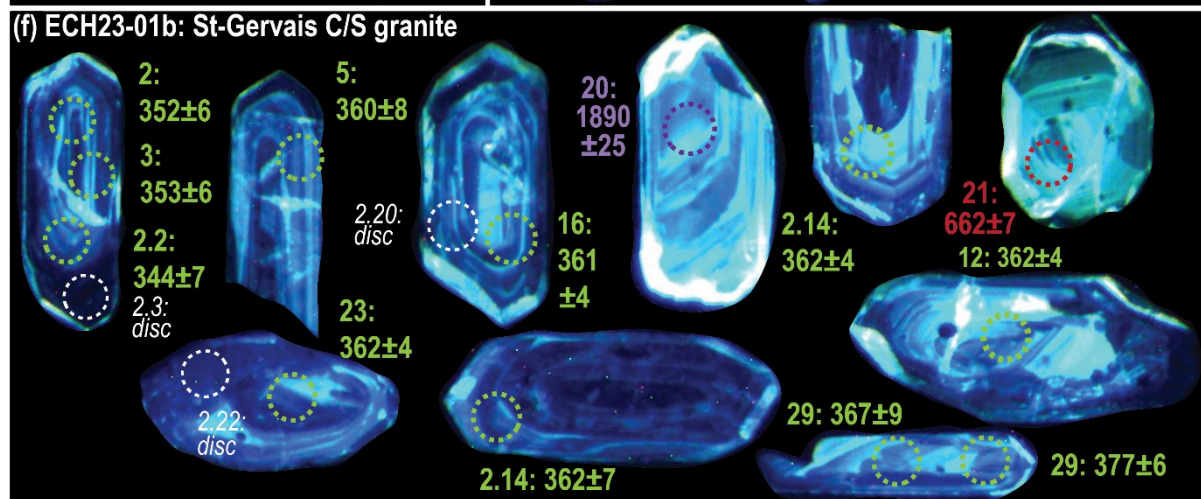
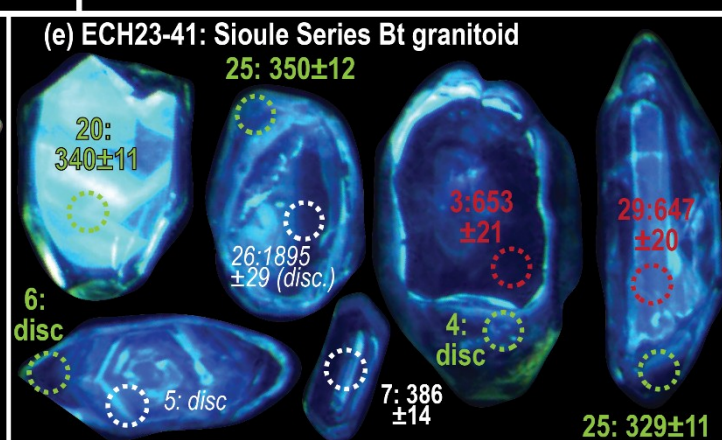
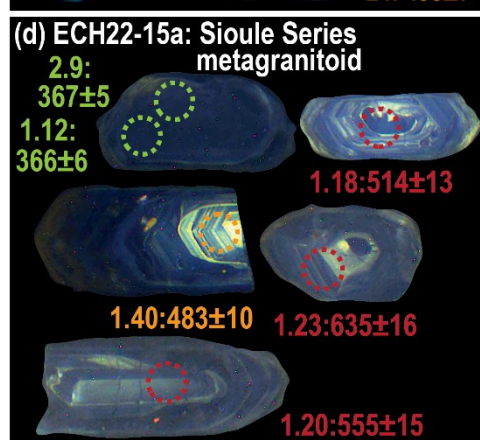
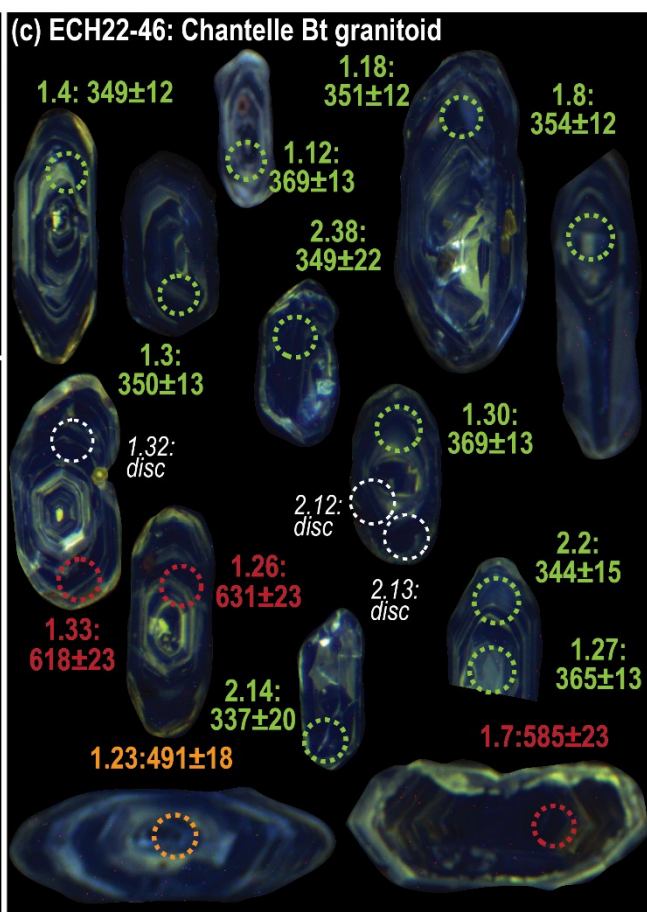
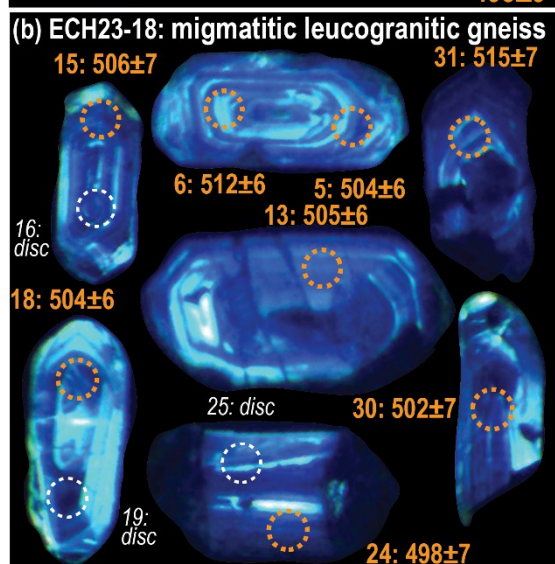
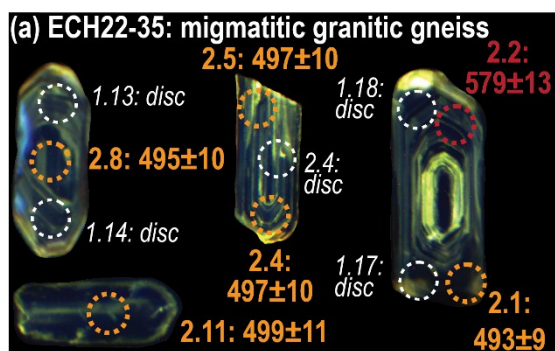
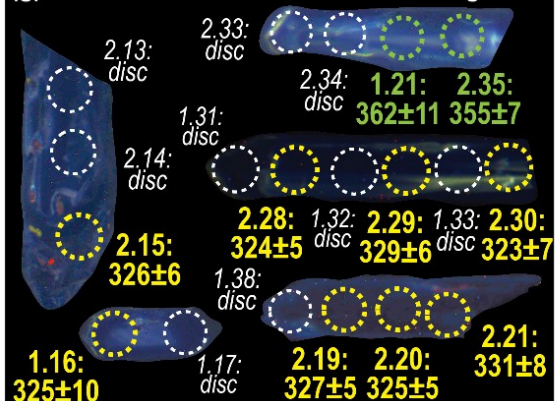


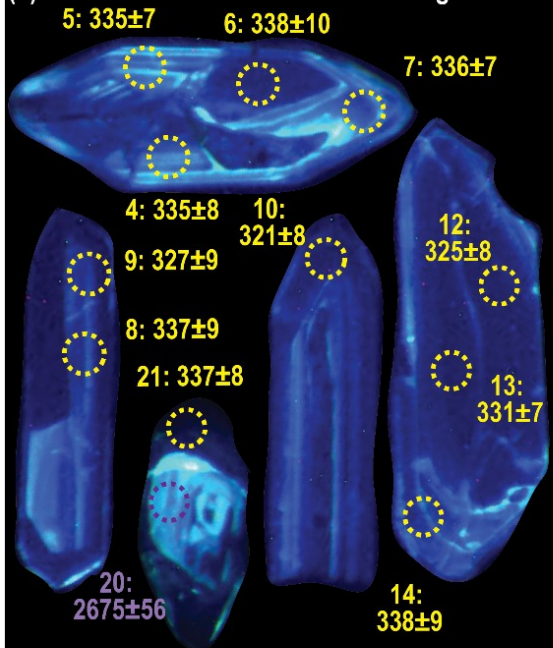
Fig. S4: Total alkali versus silica diagram for (a) (meta-) plutonic rocks (Wilson, 1989) and (b) volcanic rocks (Le Bas et al., 1986) from the Sioule region. Abbreviations: Fm. - Formation.



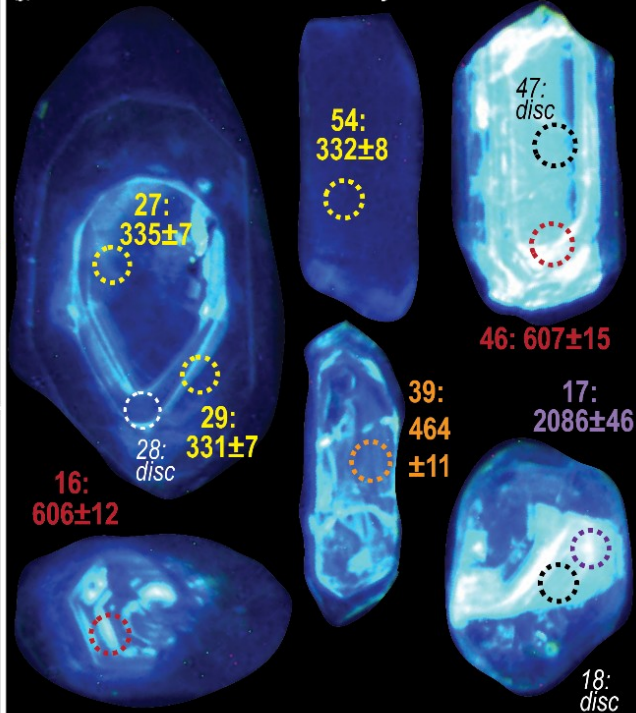
(g) ECH22-16: Pouzol-Servant Bt microgranite



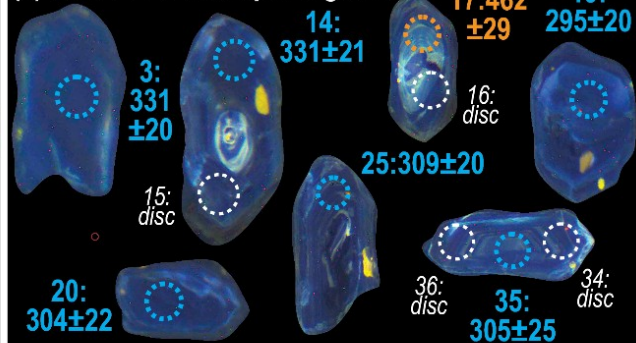
(h) ECH23-10: Pouzol-Servant Bt microgranite



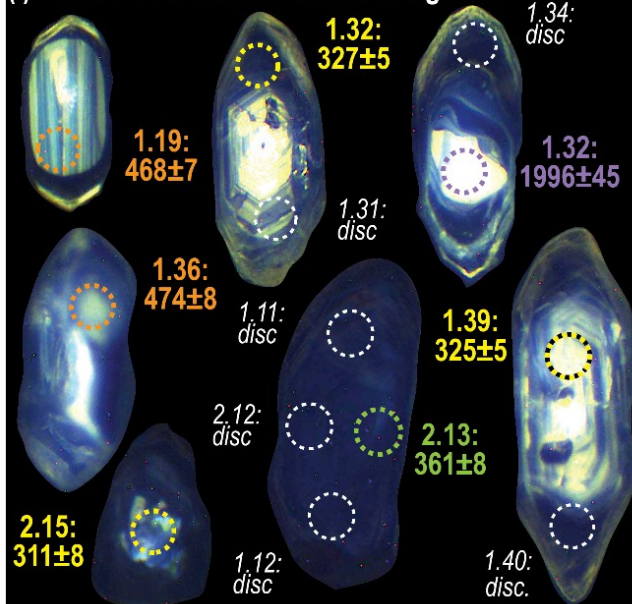
(j) ECH23-27: Manzat Fm. trachy-dacite tuff



(k) ECH22-44: Champs Bt granite



(i) ECH22-02: Colettes Li-mica-Crd granite



(l) ECH23-07a: Châteuneuf trachy-dacite tuff

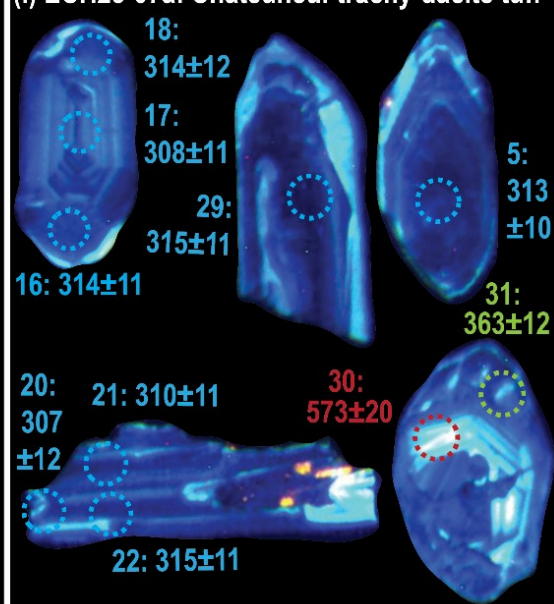
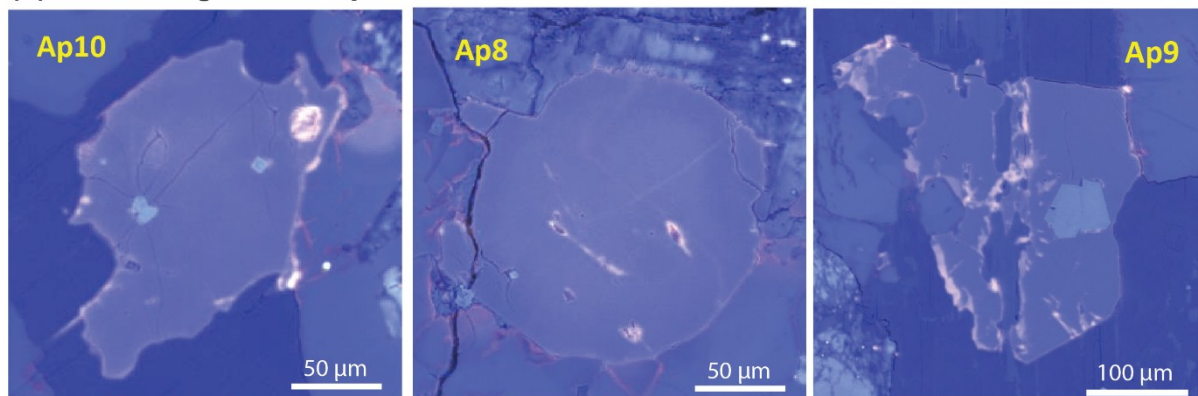


Fig. S5: Representative cathodoluminescence images of zircon grains from Sioule (meta)igneous rocks. Locations of LA-ICP-MS analytical spots are shown, along with their corresponding analysis numbers and associated $^{206}\text{Pb}/^{238}\text{U}$ dates (or $^{207}\text{Pb}/^{206}\text{Pb}$ dates for purple analyses). Date uncertainties are reported at the 2σ level.

(a) Colettes granite - apatite - Col2



(b) Beauvoir microgranite enclave - apatite - P51

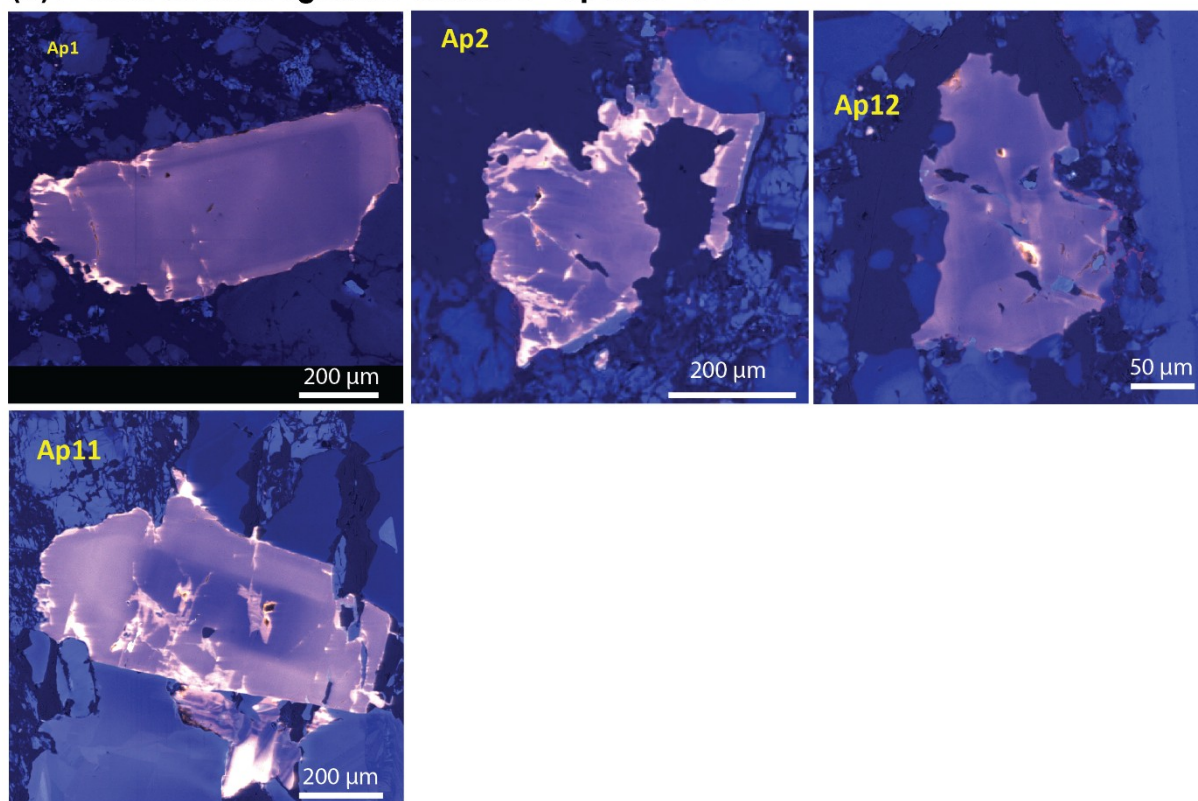


Fig. S6: Representative cathodoluminescence images of apatite grains from the Colettes granites and Beauvoir microgranite enclave that were analyzed for their U-Pb isotopic compositions.

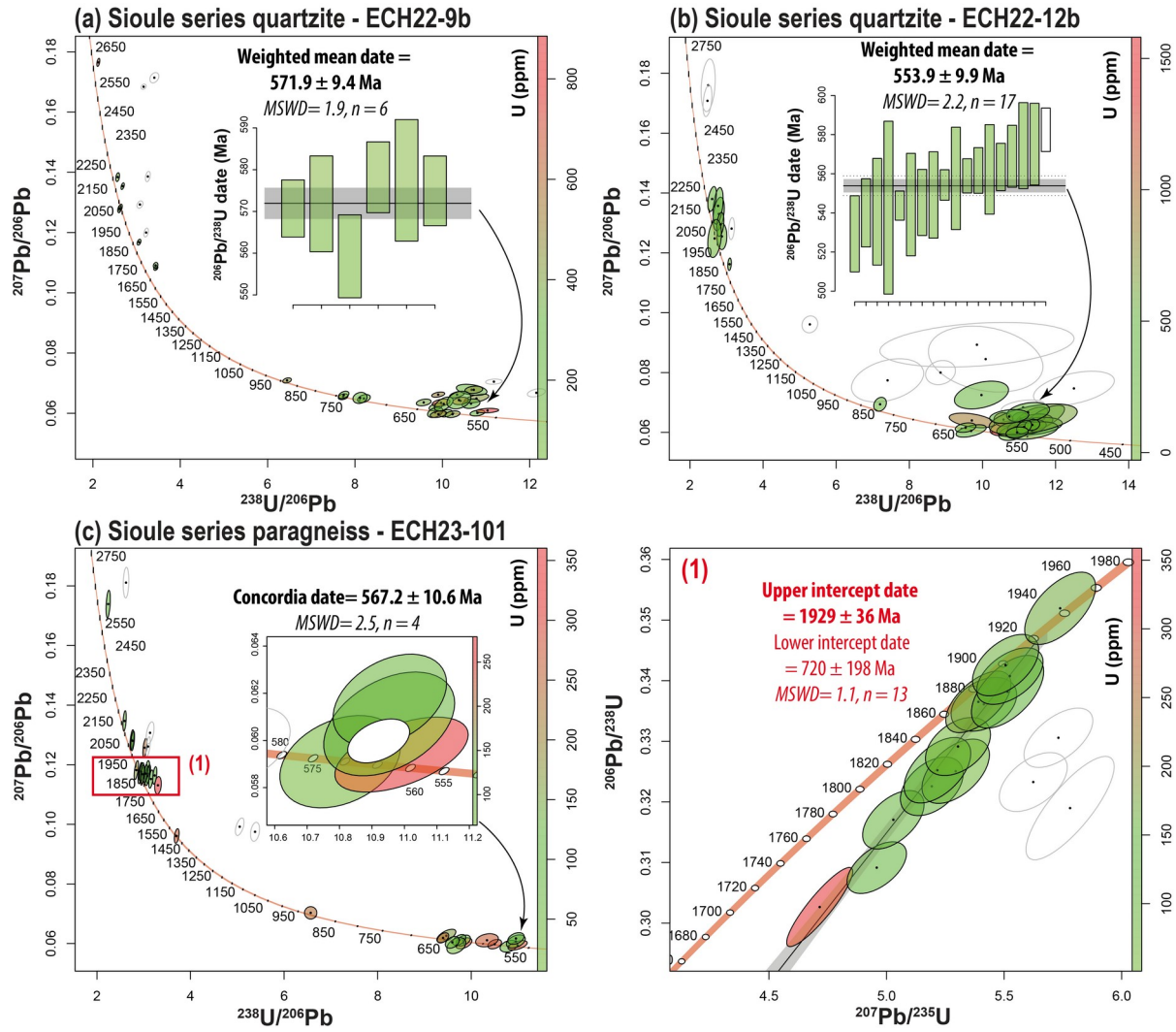


Fig. S7: U-Pb compositions of detrital zircon grains from metasedimentary rocks of the mica schist (a) and paragneiss (b-c) units of the Sioule Series. Inset diagrams show either $^{206}\text{Pb}/^{238}\text{U}$ date distributions (a-b) or a zoomed-in Tera-Wasserburg plot (c) highlighting the youngest detrital zircon dates and corresponding maximum depositional ages. Diagram (1) in panel (c) displays a close-up of the main Paleoproterozoic zircon population identified in sample ECH23-101, along with calculated intercept dates in a Wetherill concordia plot. Ellipses, error bars, and dates are reported at 2σ . Empty ellipses correspond to analyses with a degree of concordance $< 90\%$ and were excluded from the histogram and KDE diagrams in Fig. 8.

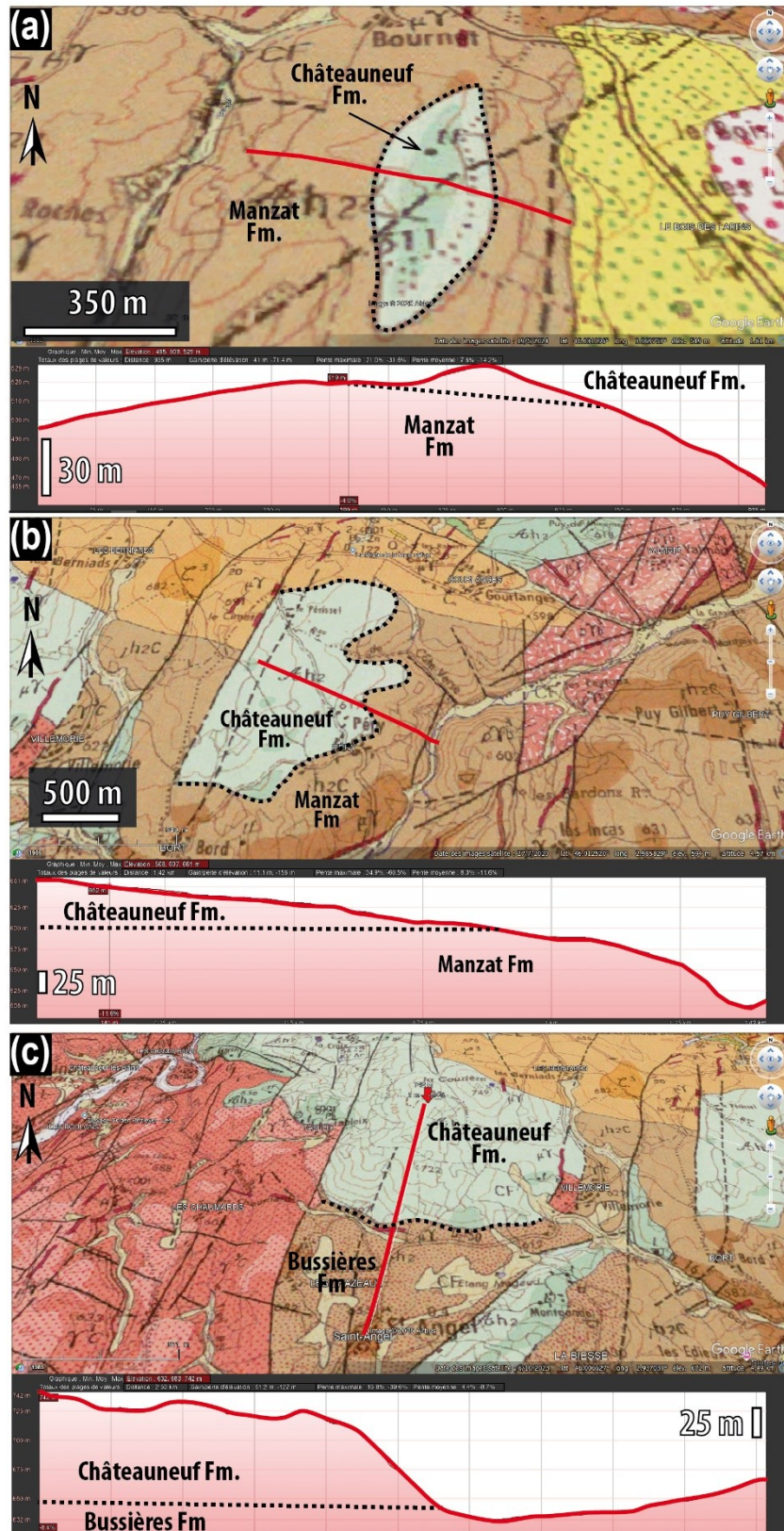


Fig. S8: Topographic profiles across the transition between the volcanic-sedimentary rocks of the Châteauneuf and Manzat Formations, constructed using Google Earth and 1:50,000 BRGM geological maps (Hottin et al., 1989). The profiles consistently show the Châteauneuf Formation overlying the Manzat Formation, supporting the interpretation of an older age for the latter.

References

- Black, L.P., Kamo, S.L., Allen, C.M., Davis, D.W., Aleinikoff, J.N., Valley, J.W., Mundil, R., Campbell, I.H., Korsch, R.J., Williams, I.S., others, 2004. Improved $^{206}\text{Pb}/^{238}\text{U}$ microprobe geochronology by the monitoring of a trace-element-related matrix effect; SHRIMP, ID-TIMS, ELA-ICP-MS and oxygen isotope documentation for a series of zircon standards. *Chem. Geol.* 205, 115–140.
- Carignan, J., Hild, P., Mevelle, G., Morel, J., Yeghicheyan, D., 2001. Routine analyses of trace elements in geological samples using flow injection and low pressure on-line liquid chromatography coupled to ICP-MS: a study of geochemical reference materials BR, DR-N, UB-N, AN-G and GH. *Geostand. Newsl.* 25, 187–198. <https://doi.org/10.1111/j.1751-908X.2001.tb00595.x>
- Carr, P.A., Zink, S., Bennett, V.C., Norman, M.D., Amelin, Y., Blevin, P.L., 2020. A new method for U-Pb geochronology of cassiterite by ID-TIMS applied to the Mole Granite polymetallic system, eastern Australia. *Chem. Geol.* 539, 119539. <https://doi.org/10.1016/j.chemgeo.2020.119539>
- Carr, P.A., Mercadier, J., Harlaux, M., Romer, R.L., Moreira, E., Legros, H., Cuney, M., Marignac, C., Cauzid, J., Salsi, L., Lecomte, A., Rouer, O., Peiffert, C., 2021. U/Pb geochronology of wolframite by LA-ICP-MS; mineralogical constraints, analytical procedures, data interpretation, and comparison with ID-TIMS. *Chem. Geol.* 584. <https://doi.org/10.1016/j.chemgeo.2021.120511>
- Carr, P.A., Moreira, E., Neymark, L., Norman, M.D., Mercadier, J., 2023. A LA-ICP-MS Comparison of Reference Materials Used in Cassiterite U-Pb Geochronology. *Geostand. Geoanalytical Res.* 47, 67–87. <https://doi.org/https://doi.org/10.1111/ggr.12469>
- Chew, D.M., Petrus, J.A., Kamber, B.S., 2014. U-Pb LA-ICPMS dating using accessory mineral standards with variable common Pb. *Chem. Geol.* 363, 185–199. <https://doi.org/10.1016/j.chemgeo.2013.11.006>
- Cuney, M., Marignac, C., Weisbrod, A., 1992. The Beauvoir topaz-lepidolite albite granite (Massif Central, France); the disseminated magmatic Sn-Li-Ta-Nb-Be mineralization. *Econ. Geol.* 87, 1766–1794. <https://doi.org/https://doi.org/10.2113/gsecongeo.87.7.1766>
- Gain, S.E.M., Gréau, Y., Henry, H., Belousova, E., Dainis, I., Griffin, W.L., O'reilly, S.Y., 2019. Mud tank zircon: long-term evaluation of a reference material for U-Pb dating, Hf-isotope analysis and trace element analysis. *Geostand. Geoanalytical Res.* 43, 339–354.
- Hottin, A.M., Belin, J., Bois, J., Deyrieux, G., Morice, E., Périchaud, J.J., D'Arcy, D., 1989. Carte géol. France (1/50000), feuille SAINT-GERVAIS-D'Auvergne (668). BRGM, Orléans.
- Jochum, K.P., Weis, U., Stoll, B., Kuzmin, D., Yang, Q., Raczek, I., Jacob, D.E., Stracke, A., Birbaum, K., Frick, D.A., others, 2011. Determination of reference values for NIST SRM 610-617 glasses following ISO guidelines. *Geostand. Geoanalytical Res.* 35, 397–429.
- Le Bas, M.J., Le Maitre, R.W., Streckeisen, A., Zanettin, B., on the Systematics of Igneous Rocks, I.S., 1986. A chemical classification of volcanic rocks

- based on the total alkali-silica diagram. *J. Petrol.* 27, 745–750.
- Paton, C., Woodhead, J.D., Hellstrom, J.C., Hergt, J.M., Greig, A., Maas, R., 2010. Improved laser ablation U-Pb zircon geochronology through robust downhole fractionation correction. *Geochemistry, Geophys. Geosystems* 11, Q0AA06. <https://doi.org/10.1029/2009GC002618>
- Petrus, J.A., Kamber, B.S., 2012. VizualAge: A novel approach to laser ablation ICP-MS U-Pb geochronology data reduction. *Geostand. Geoanalytical Res.* 36, 247–270. <https://doi.org/https://doi.org/10.1111/j.1751-908X.2012.00158.x>
- Rocher, O., Ballouard, C., Richard, A., Monnier, L., Carr, P., Laurent, O., Khebabza, Y., Lecomte, A., Bouden, N., Villeneuve, J., Barré, B., Fullenwarth, P., Leisen, M., Mercadier, J., 2024. Unravelling the magmatic and hydrothermal evolution of rare-metal granites through apatite geochemistry and geochronology: The Variscan Beauvoir granite (French Massif Central). *Chem. Geol.* 670, 122400. <https://doi.org/https://doi.org/10.1016/j.chemgeo.2024.122400>
- Schmitz, M.D., Bowring, S.A., Ireland, T.R., 2003. Evaluation of Duluth Complex anorthositic series (AS3) zircon as a U-Pb geochronological standard: New high-precision isotope dilution thermal ionization mass spectrometry results. *Geochim. Cosmochim. Acta* 67, 3665–3672.
- Schoene, B., Bowring, S.A., 2006. U-Pb systematics of the McClure Mountain syenite: thermochronological constraints on the age of the $^{40}\text{Ar}/^{39}\text{Ar}$ standard MMhb. *Contrib. to Mineral. Petrol.* 151, 615. <https://doi.org/10.1007/s00410-006-0077-4>
- Tapster, S., Bright, J.W.G., 2020. High-precision ID-TIMS cassiterite U-Pb systematics using a low-contamination hydrothermal decomposition: implications for LA-ICP-MS and ore deposit geochronology. *Geochronology* 2, 425–441. <https://doi.org/10.5194/gchron-2-425-2020>
- Thomson, S.N., Gehrels, G.E., Ruiz, J., Buchwaldt, R., 2012. Routine low-damage apatite U-Pb dating using laser ablation-multicollector-ICPMS. *Geochemistry, Geophys. Geosystems* 13, Q0AA21. <https://doi.org/10.1029/2011GC003928>
- Webb, P., Wiedenbeck, M., Glodny, J., 2020. G-Chron 2019-Round 1: An International Proficiency Test for U-Pb Geochronology Laboratories; Report on the 2019 Round of G-Chron based on Palaeozoic Zircon Rak-17 (Distribution: September 2019). GFZ German Research Centre for Geosciences, Potsdam. <https://doi.org/https://doi.org/10.48440/GFZ.b103-21061>
- Webb, P., Wiedenbeck, M., Glodny, J., 2021. G-Chron 2021 – Round 2 — An International Proficiency Test for U-Pb Geochronology Laboratories — Report on the 2021 Round of G-Chron based on Archean Zircon Kara-18 22.
- Wiedenbeck, M., Allé, P., Corfu, F., Griffin, W. I., Meier, M., Oberli, F., Quadrt, A. Von, Roddick, J. c., Spiegel, W., 1995. Three Natural Zircon Standards for U-Th-Pb, Lu-Hf, Trace Element and REE Analyses. *Geostand. Newsl.* 19, 1–23. <https://doi.org/10.1111/j.1751-908X.1995.tb00147.x>
- Wilson, B.M., 1989. *Igneous petrogenesis: a global tectonic approach*. Springer Science & Business Media.

Woodhead, J.D., Hergt, J.M., 2000. Pb-isotope analyses of USGS reference materials. *Geostand. Newsl.* 24, 33–38.